



## Electrodeposited white bronzes on brass: Corrosion in 3.5 % sodium chloride solution

E. Berretti<sup>a</sup>, N. Calisi<sup>b,c</sup>, A. Capaccioli<sup>d</sup>, L. Capozzoli<sup>a</sup>, A.M.S. Hamouda<sup>e</sup>, A. Giaccherini<sup>f,g</sup>,  
W. Giurlani<sup>g</sup>, A. Ienco<sup>a</sup>, S. Martinuzzi<sup>g</sup>, M. Innocenti<sup>g</sup>, U. Waware<sup>e,\*</sup>, S. Virtanen<sup>h</sup>, G. Zangari<sup>i</sup>,  
R. Ahmed<sup>i</sup>, A. Lavacchi<sup>a,\*</sup>

<sup>a</sup> CNR-ICCOM, Via Madonna del Piano 10, 50019, Sesto Fiorentino (Florence), Italy

<sup>b</sup> Industrial Engineering Department, University of Florence, Via di S. Marta 3, 50139, Florence, Italy

<sup>c</sup> INSTM, Via G. Giusti, 9, 50121, Florence, Italy

<sup>d</sup> ITALFIMET Srl, Via XXV Aprile 88, 52048, Monte San Savino (Arezzo), Italy

<sup>e</sup> Department of Mechanical and Industrial Engineering, College of Engineering, Building B09, Qatar University, Doha, Qatar

<sup>f</sup> Department of Earth Sciences, University of Florence, Via La Pira 4, 50121, Florence, Italy

<sup>g</sup> Chemistry Department, University of Florence, Via della Lastruccia 3, Florence, Italy

<sup>h</sup> Materials Science Department, University of Erlangen-Nuremberg, Martenstr. 7, D-91058, Erlangen, Germany

<sup>i</sup> University of Virginia, Materials Science and Engineering, 351 McCormick Rd., Charlottesville, VA, 22904, USA

### ARTICLE INFO

#### Keywords:

Bronze  
Electrodeposited films  
Marine corrosion  
XPS  
XRD  
SEM

### ABSTRACT

White bronzes are electrodeposited coatings applied on brass as surface finishes. We report a comparative study on the corrosion resistance in chloride aqueous environment of two white bronzes, a Zn-bearing and a Zn-free. Corrosion tests showed that both materials provide protection to brass, but the Zn-free is more cathodic and performs better in the test environment, following a different corrosion mechanism. We also explored the effect of the coating thickness on the corrosion parameters. We found that the more cathodic OCPs were achieved with coatings exceeding 1  $\mu\text{m}$ , while the 0.5  $\mu\text{m}$  coatings show OCPs closer to the brass substrate.

### 1. Introduction

White bronzes are electrodeposited coatings consisting of Cu-Sn (Zn). Recently, they have found an extensive application as an alternative to electroplated Nickel [1–5]. Together with Ni coatings, they share excellent corrosion and wear resistance. For this reason, white bronzes have been widely employed as intermediate layers in the applications that require stability of the appearance (long-lasting brightness and no change of colour in time), e.g. in fashion goods [6]. White bronzes coatings are also good electric conductors that are hard to oxidize, even in an aggressive sulfuric environment [7,8]. For these properties, they have been proposed as a viable alternative to bare Cu or Zn coatings for the protection of electric and electronic components for automotive [9,10]. Moreover, a significant research effort on ternary white bronzes deposition has been recently deployed as these materials are useful precursors for the synthesis of kesterite (CZTS,  $\text{Cu}_2\text{ZnSnS}_4$ ) semiconductors. This has enabled the fabrication of photovoltaic cells with only earth-abundant materials [7,8,11–14] and more than 10 % efficiency.

While kesterite precursors are usually deposited from acid electrolytes, the most popular solutions for white bronzes deposition are alkaline; in industrial processes, the most galvanic bath employs cyanides as complexing agents [15–18]. With the addition of proper additives, cyanide electrolytes grow smooth and bright deposits with mirror-like surface finishing. Additionally, cyanide provides performance stability and accurate control of the composition of the electrodeposited films under heavy-duty loads and long-term operations. The main disadvantage of cyanide is toxicity, that requires complex handling protocols and well established and documented waste treatment procedures [19,20]. This study focuses on white bronzes deposited from cyanide electrolytes.

Ternary white bronzes containing Cu, Zn and Sn (Copper Zinc Tin, or CZT) are widely used in the electroplating industry for two main reasons: i) Zn containing bronzes have shiny surfaces even at a tin concentration significantly lower than 20 % wt. [20–22] and ii) they deposit 40 % faster than the corresponding Cu-Sn binary alloys [21]. Moreover, Zn-bearing coatings are usually less porous and brighter with a nickel-like appearance that compares to the pewter-like colour of

\* Corresponding authors.

E-mail addresses: [usaware@qu.edu.qa](mailto:usaware@qu.edu.qa) (U. Waware), [alavacchi@iccom.cnr.it](mailto:alavacchi@iccom.cnr.it) (A. Lavacchi).

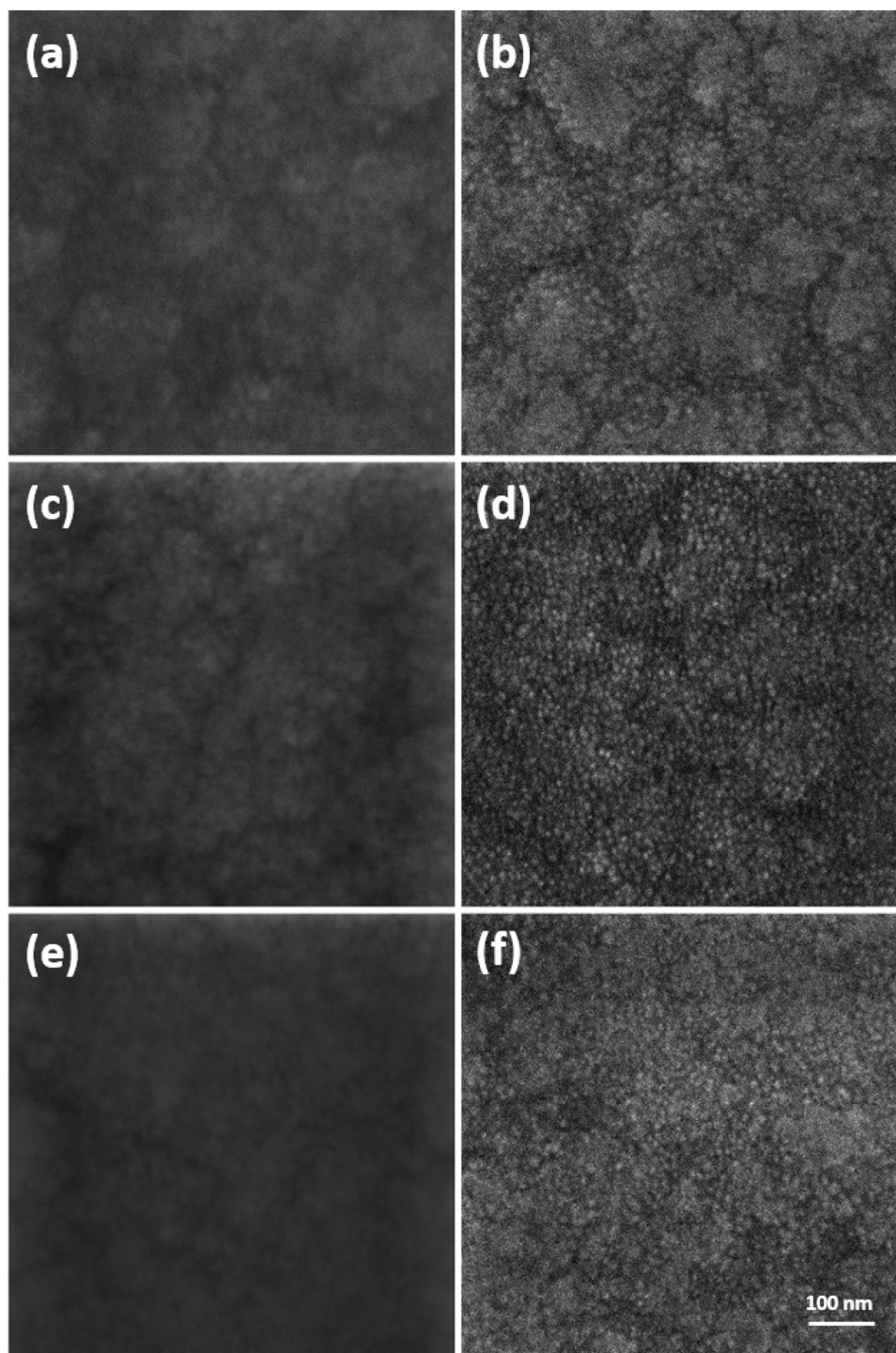


Fig. 1. 400kx SEM images of the surface morphology of Zn-bearing white bronze (a,c,e, left column, respectively 0.5, 1.0 and 1.5  $\mu\text{m}$  thick), and Zn-free white bronze (b, d, f, right column, respectively 0.5, 1.0 and 1.5  $\mu\text{m}$  thick).

binary Cu-Sn coatings [22,23]. On the other side, high tin binary bronze is harder compared to ternary alloys, making them a favourite choice if resistance to scratch, wear and erosion are required.

Generally, CZT white bronzes show better corrosion resistance in aqueous environment in standard conditions with respect to naval brasses [3,24–26]. This behaviour is due to the formation of a tin (IV) passivation layer consisting of insoluble tin oxo-hydroxides. These oxidized tin species limit the corrosion rate in non-complexing aqueous media [27]. When more than 10 % of tin is incorporated, white bronzes are hard and exceed the corrosion resistance of brass. Often in practical

applications, up to 20 % and more tin is added to improve corrosion resistance [28,29]. Electrodeposited white bronzes with 50 wt. % Cu, 25 wt. % Zn and 25 wt.% Sn still show fast corrosion rates when in contact with marine atmosphere [30,31], fastly uncovering the substrate materials.

This work focuses on the corrosion performance, the structure and the morphology of two classes of white bronze deposited on brass, a CZT ternary alloy (ca. 55 %wt. Cu, 23 % wt. Sn and 22 % wt. Zn) and a high tin zinc-free coating (ca. 63 %wt. Cu, 36 %wt. Sn, 1 %wt. Pd). We selected brass as a substrate for its applications as a cheap alternative

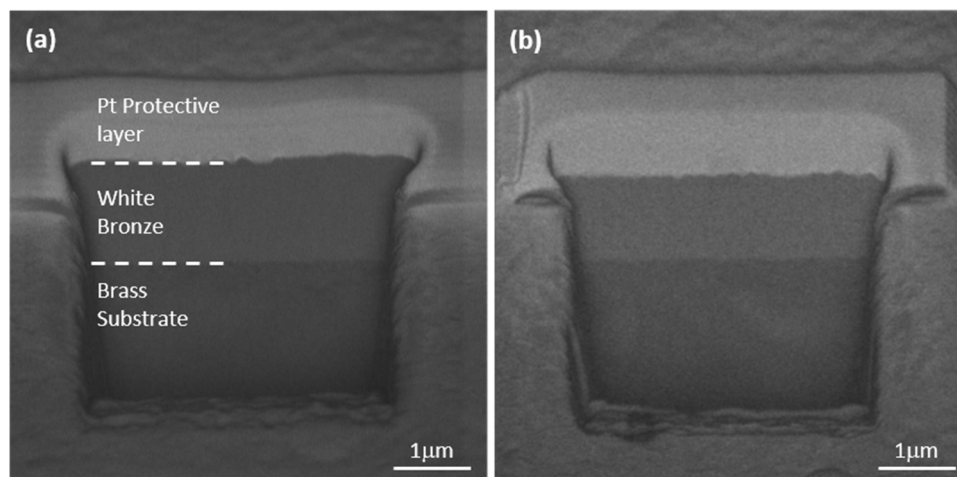


**Fig. 2.** FIB cross-sections of (a) the 1.5  $\mu\text{m}$  thick Zn-bearing white bronze and (b) the 1.5  $\mu\text{m}$  Zn-free white bronze acquired by the in-beam backscattered electron detector.

**Table 1**

Thickness of the Zn-free and Zn-bearing bronze films determined by FIB/SEM cross-sections.

Nominal thickness ( $\mu\text{m}$ )	Zn-bearing White Bronze measured thickness ( $\mu\text{m}$ )	Zn-free White Bronze measured thickness ( $\mu\text{m}$ )
0,5	0,47	0,48
1	1,13	1,02
1,5	1,70	1,47

technical interest, limited information of the corrosion performance of electrodeposited white bronzes on brass with  $> 35\%$  wt. Sn is reported in the literature. Brass protection with white bronze, especially with high-tin ones has the potential to limit degradation, preserving physical properties and extending the service life of the components.

## 2. Materials and methods

### 2.1. White bronzes electrodeposition

Zn-bearing and Zn-free layers were deposited by galvanostatic electrodeposition (plating electronic GmbH with output 10 V/10A power supply), using brass (67 % Cu, 33 % Zn) substrates as working electrodes (WE), and a mesh made of mixed conductive oxides as a counter electrode (CE). The CE was bent in a cylindrical shape, to make contact with the cylindrical inner walls of a 1-litre beaker, while the WE was placed in the centre of the vessel (distance between electrodes 5 cm, depth from the surface about 3 cm). Two different galvanic baths were used to produce the samples:

- o The galvanic bath, commercialised by ITALFIMET (Monte San Savino, AR, Italy), for the production of Zn-bearing white bronze coatings. Deposits were grown using a current density of  $2 \text{ A/dm}^2$  and a deposition time of 2, 4, and 6 min to obtain a deposit thickness of 0.5  $\mu\text{m}$ , 1.0  $\mu\text{m}$  and 1.5  $\mu\text{m}$ , respectively;
- o A modified version of the previous bath, also produced in ITALFIMET's lab, to produce Zn-free white bronze layers. Deposits were produced using a current density of  $2 \text{ A/dm}^2$  and a deposition time of 4, 8, and 10 min to grow the film to the thickness of 0.5  $\mu\text{m}$ , 1.0  $\mu\text{m}$  and 1.5  $\mu\text{m}$ , respectively.

### 2.2. FIB/SEM measurements

SEM image acquisition, ionic imaging, cross-sectioning and EDX analysis were performed using a TESCAN GAIA 3 FIB/SEM microscope equipped with an EDAX Octane Elect Super EDX detector. The microscope hosts a 30 kV Triglav electron column, and a Cobra Focused Gallium Ion Beam column. To measure the thickness of the coatings, we employed a FIB cross-section milling procedure. A protective ( $> 1.5 \mu\text{m}$  thick) layer of Pt was applied before trench milling to avoid edge rounding (The topmost whitish layer visible in Fig. 2). SEM images for morphology investigation were acquired using the in-beam secondary electron detector. In contrast, for the cross-sections, the image acquisition was performed by in-beam backscattered electron detector to

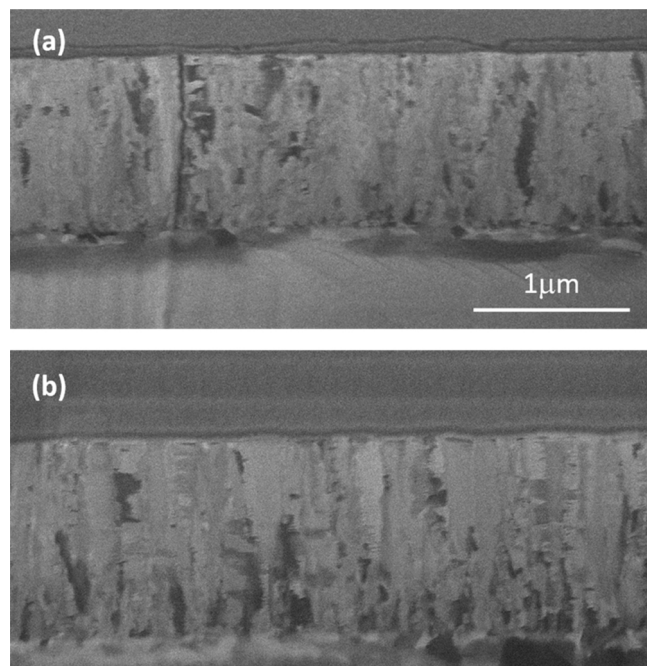


**Fig. 3.** Ionic pictures of two 1.5  $\mu\text{m}$  coatings: (a) Zn-bearing white bronze and (b) Zn-free white bronze, same scalebar for both the images Central columnal layer refers to white bronze deposits, while topmost darker and bottom whiter layers are respectively the Pt protection layer and the substrate.

for the fabrication of DC and RF electronic connectors for the automotive industry and as a substrate for inexpensive accessory for the fashion industry. In both applications, the occasional contact with NaCl rich atmosphere may occur, generating oxidation phenomena detrimental to the functional properties. Moreover, despite the potential

**Table 2**

Compositional results (all elements) of the EDX analysis on both Zn and Zn-free white bronzes. EDX measurements performed at 12 kV.

Sample	Element	Weight %			Atomic %			Error %		
		0.5 $\mu\text{m}$	1.0 $\mu\text{m}$	1.5 $\mu\text{m}$	0.5 $\mu\text{m}$	1.0 $\mu\text{m}$	1.5 $\mu\text{m}$	0.5 $\mu\text{m}$	1.0 $\mu\text{m}$	1.5 $\mu\text{m}$
<b>Zn-bearing Bronze</b>	C	4.80	5.10	3.10	22.80	23.55	15.68	10.21	10.19	10.56
	O	1.33	1.60	1.36	4.74	5.56	5.16	8.49	8.34	8.36
	Cu	46.11	47.61	48.23	41.36	41.59	46.04	4.15	4.00	4.06
	Zn	20.87	20.82	21.47	18.19	17.68	19.92	7.33	7.32	7.39
	Sn	26.89	24.87	25.84	12.91	11.63	13.21	3.12	3.09	2.98
<b>Zn-free Bronze</b>	C	1.84	1.29	2.10	10.47	7.40	11.60	43.13	12.28	11.02
	O	0.70	1.26	1.25	3.01	5.47	5.20	9.86	8.38	8.39
	Cu	60.74	59.70	59.85	65.34	65.01	62.55	4.94	5.01	4.96
	Pd	0.61	1.66	1.12	0.39	1.08	0.70	30.00	7.60	9.13
	Sn	36.10	36.09	35.68	20.79	21.04	19.96	3.06	2.76	2.77

**Table 3**

Compositional results (metals only) of the EDX analysis on both Zn and Zn-free white bronzes. EDX measurements performed at 12 kV.

Sample	Element	Weight %			Atomic %			Error %		
		0.5 $\mu\text{m}$	1.0 $\mu\text{m}$	1.5 $\mu\text{m}$	0.5 $\mu\text{m}$	1.0 $\mu\text{m}$	1.5 $\mu\text{m}$	0.5 $\mu\text{m}$	1.0 $\mu\text{m}$	1.5 $\mu\text{m}$
<b>Zn-bearing Bronze</b>	Cu	48.77	50.57	50.16	56.56	58.05	57.73	4.18	4.02	4.06
	Zn	22.95	23.11	23.00	25.88	25.78	25.73	7.49	7.50	7.50
	Sn	28.28	26.32	26.84	17.56	16.17	16.54	3.09	3.02	2.96
<b>Zn-free Bronze</b>	Cu	62.50	61.37	62.14	75.66	74.70	75.36	4.97	5.03	4.98
	Pd	0.61	1.71	0.79	0.44	1.24	0.57	29.88	7.65	26.08
	Sn	36.88	36.92	37.07	23.90	24.06	24.07	3.04	2.78	2.81

enhance the contrast between the substrate and the coatings, using both electron and ionic probes. SEM cross-section imaging was performed in immersion mode (UH Resolution mode), with an e-beam acceleration of 5 kV. EDS data acquisition was performed using a 12 kV beam to sample only the electrodeposited layer and to permit X-ray typical emission of all its constituent elements (Pd, Zn, Cu and Sn). Ionic images were acquired using a five pA Ga<sup>+</sup> current accelerated at 30 kV. FIB and SEM images were collected using a 55° sample tilt. To correct the thickness of the deposited film, the real thickness was achieved multiplying by 1/cos (35°).

### 2.3. XPS measurements

XPS measurements were carried out on a Kratos AXIS Ultra DLD with an Al K $\alpha$  monochromatic source to produce X-Rays (15 kV, 20 mA). Preliminary full surveys of the samples were performed at 160 eV pass energy, while the high-resolution spectra acquisition was performed at pass energy of 20 eV. Sputtering cycles were performed by the in-built Ar ion gun, adopting two 120 s cycles with an accelerating potential of 3 kV. These sputtering cycles were needed to uncover the metallic surface of the coatings, which was initially enfolded by a carbonous layer hindering metals determination. Data were analyzed using the dedicated software CasaXPS (Figs. S13 & 4). Spectra were calibrated shifting the aliphatic component of carbon to 285 eV, and for the fitting of the peaks, mixed Gaussian-Lorentzian components were used.

### 2.4. XRD experiments

X-ray powder diffraction (PXRD) scans were acquired at room temperature with a PANalytical X'PERT PRO diffractometer, employing CuK $\alpha$  radiation ( $\lambda = 1.54187 \text{ \AA}$ ) and a PW3088/60-graded multilayer parabolic X-ray mirror for Cu radiation. The produced coatings were used directly as samples for the acquisition. The diffractograms were acquired in the 2 $\theta$  range from 5.0 to 120.08, using a continuous scan mode with an acquisition step size of  $2\theta = 0.02638$  and a counting time

of 49.5 s. The qualitative assignment of the peaks has been performed using the QualX2 software and the COD database [32]. The peak fit of the diffractograms has been carried out employing the GSAS2 software [33] holding the positions of the peaks to the ones expected from assigned phases.

### 2.5. Colour measurements

The UV–vis–NIR diffuse reflectance spectrum of the coated substrates was measured using an Agilent Cary 300 spectrophotometer, equipped with a Labsphere PELA-1050 integration sphere. Diffuse Reflectance Spectroscopy (DRS) spectra were recorded in the range 340–830 nm, at a step of 10 nm, counting 0.2 s per step. The relative reflectance was calculated employing a reference sample with a standard white diffuse reflectance spectrum (Spectralon [34]). We converted the relative DRS spectra to Lab colour coordinates using the “Multispectra” [35] software developed by our group and based on the colour match library [36]. This procedure implements the Lab 1976 recommendation defined by CIE [37] and allows for the calculation of the colour distances. According to Lab 1976, the difference in colour “sensation” ( $\Delta E$ ) is reported in the text.

### 2.6. Corrosion measurements

1  $\mu\text{m}$  thick coatings were subjected to Open Circuit Potential (OCP) measurements using a benchtop voltmeter, by periodically recording the potential between the coating surface and a Metrohm Ag/AgCl electrode. A 0.62 M NaCl (3.5 wt.% aqueous solution) was used as the electrolyte for all the corrosion measurements. The pH of the solution was adjusted between 8.1 and 8.4, using NaOH to match the pH conditions of seawater closely [30]. The samples were held inside a custom made cell, exposing about 0.2 cm<sup>2</sup> surface to the electrolytic solution.

Polarization tests were performed using a Gamry PCI-4 300 potentiostat/galvanostat, exposing a circular surface of the sample (3.5 mm diameter) as working electrode (WE), a Pt mesh as the counter electrode (CE) and a standard calomel electrode (SCE) as a reference

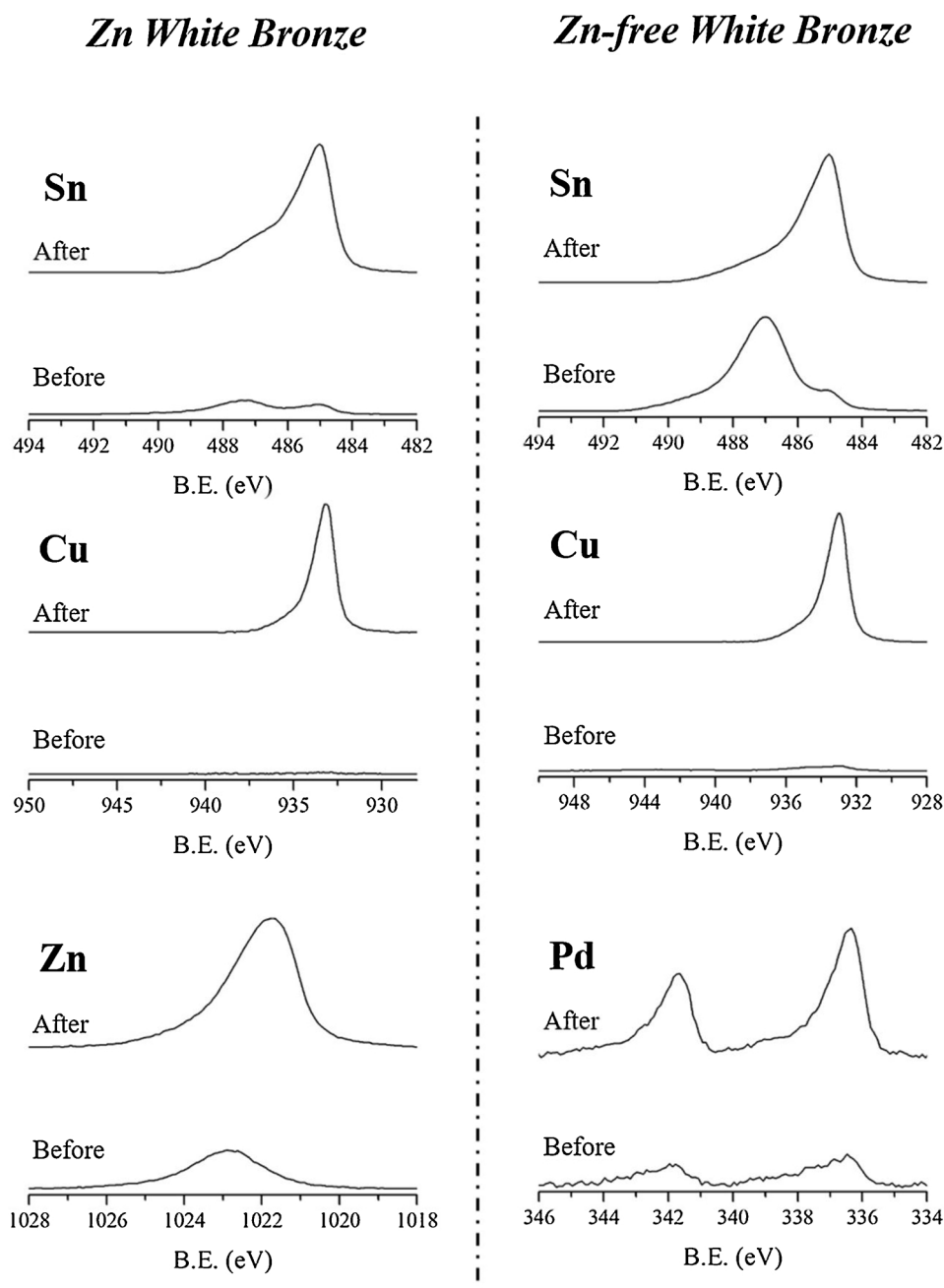


Fig. 4. High-resolution XPS spectra of the 1  $\mu\text{m}$  Zn white bronze (left) and 1  $\mu\text{m}$  Zn-free white bronze (right) before and after ion sputtering. Cu 2p, Sn 3d, Zn 2p and Pd 3d regions.

electrode (RE). Potentiodynamic cycles were performed using the same potentiostat/galvanostat, starting from  $-0.05$  V vs OCP, ending at  $+1$  V vs OCP (anodic direction), and back to  $-0.3$  V vs OCP (cathodic direction), at a scan rate of  $0.5$  mV/sec. Initial OCP values were collected after 60 s.

EIS was performed on the  $1$   $\mu\text{m}$  thick samples (Zn-free, Zn-bearing) and the brass substrate using a Parstat 2273 potentiostat. The electrochemical set-up was composed by a PAR G0097 electrode holder for the WE (exposed sample surface  $1$   $\text{cm}^2$ ), a Metrohm Ag/AgCl electrode as RE and a graphite rod as CE. Tests were performed in Parstat K0047 Corrosion cell. EIS data were acquired after 1 h equilibration in the electrolyte.

All the sample surfaces were cleaned before their use by a three-step cycle consisting in a) a first rinsing with acetone, b) a second rinsing with isopropanol, c) a third rinsing using milli-q water, and d) a final

drying using a nitrogen flux.

### 3. Results and discussion

#### 3.1. SEM investigation

##### 3.1.1. Surface morphology

Fig. 1 reports the SEM images at high magnification of representative samples investigated in this study. Zn-free images show features with sizes of less than  $50$  nm. Such nanostructures are the results of the addition of polyalcohol brightener that inhibits crystal growth, favouring small crystallite size and resulting in a surface roughness much smaller than the wavelength of light [20,38–40]. The Zn-bearing bronze films, in contrast, show much less evident nanostructures. In particular, the surface appears covered by an incoherent

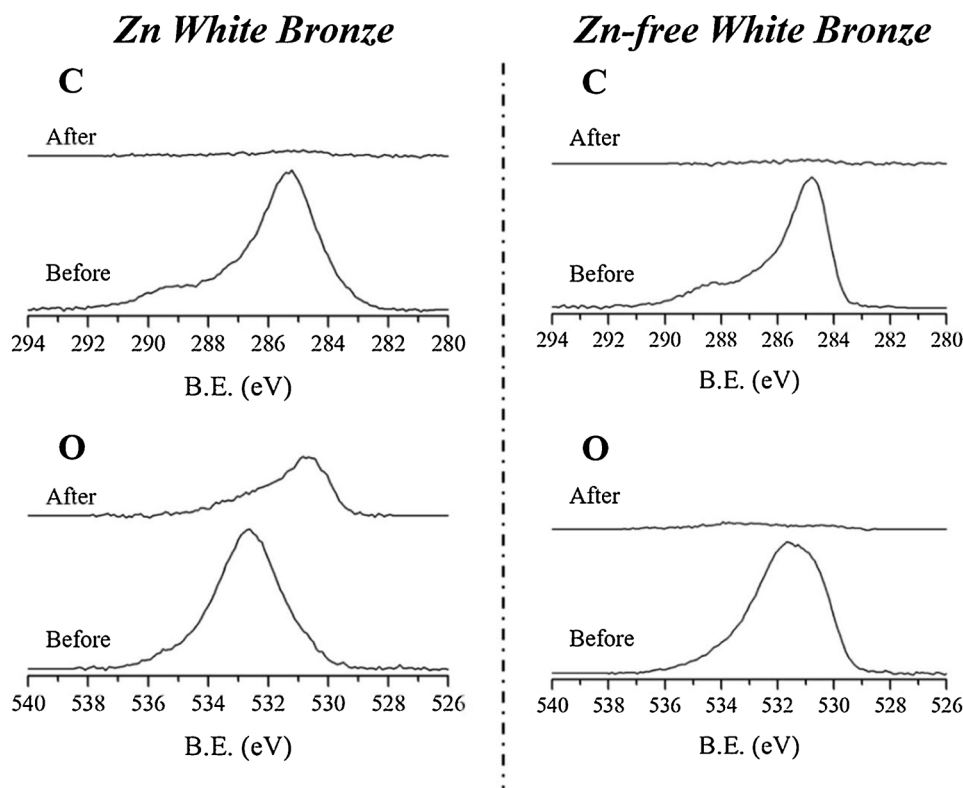


Fig. 5. High-resolution XPS spectra of the 1 $\mu$ m Zn white bronze (left) and 1 $\mu$ m Zn-free white bronze (right) before and after ion sputtering. C 1s and O 1s regions.

**Table 4**  
Surface atomic % composition of Zn white bronze and Zn-free white bronze before and after ion sputtering.

Sample	Element	Before Sputtering (% Atomic)			After Sputtering (% Atomic)		
		0.5 $\mu$ m	1.0 $\mu$ m	1.5 $\mu$ m	0.5 $\mu$ m	1.0 $\mu$ m	1.5 $\mu$ m
Zn-bearing Bronze	C	72.67	76.10	75.22	3.48	7.03	3.66
	O	20.76	18.50	19.25	11.50	11.12	12.29
	Cu	ND	ND	ND	36.12	35.80	35.36
	Zn	5.29	3.91	4.26	25.41	25.42	25.31
	Sn	1.27	1.08	1.28	23.49	20.63	23.38
Zn-free Bronze	C	47.75	51.75	52.37	0.96	0.50	1.39
	O	35.40	33.53	33.00	1.37	3.27	4.30
	Cu	4.25	4.93	4.63	74.71	74.23	70.83
	Pd	0.11	0.17	0.08	1.13	1.71	1.32
	Sn	12.49	9.61	9.92	21.83	20.29	22.16

**Table 5**  
XPS atomic ratios between a single metal and the overall metal content in Zn white bronze moreover, Zn-free white bronze before and after ion sputtering.

Sample	Element	Before Sputtering (% Atomic)			After Sputtering (% Atomic)		
		0.5 $\mu$ m	1.0 $\mu$ m	1.5 $\mu$ m	0.5 $\mu$ m	1.0 $\mu$ m	1.5 $\mu$ m
Zn-bearing Bronze	Cu	ND	ND	ND	42.5	43.7	42.1
	Zn	80.6	78.4	76.9	29.9	31.1	30.1
	Sn	19.4	21.6	23.1	27.6	25.2	27.8
Zn-Free Bronze	Cu	25.2	33.5	31.7	76.5	77.1	75.1
	Pd	0.7	1.2	0.5	1.2	1.8	1.4
	Sn	74.1	65.3	67.8	22.3	21.1	23.5

layer that, if kept under the electron beam, quickly changes in shape, suggesting high carbon contamination that cannot be removed from the surface (the topic will be explored in detail in the XPS section). This is

due to the different chemical nature of the brightening agents used in the two electrolytes, which lead to more surface impurities in the Zn-bearing bronzes, partially hiding the metal surface at high magnification.

### 3.1.2. Coating thickness

The coating thickness was measured by cross-sectioning with a Ga<sup>+</sup> ion beam in the FIB-SEM and imaging the cross-sections with primary electrons for optimal phase contrast. Pictures taken from the samples with a nominal thickness of 1.5  $\mu$ m for both the Zn-free and Zn bronzes are reported in Fig. 2; the topmost coating visible in both images is the deposited Pt protective layer, usually adopted to prevent edge rounding during FIB machining.

The measured thickness was in good agreement with what expected from the settings of the electrodeposition experiments for the Zn-free series. Minor variations between nominal and experimental thicknesses were observed for Zn-bearing white bronze coatings, especially for thicker deposits. Additionally, small differences in thickness and

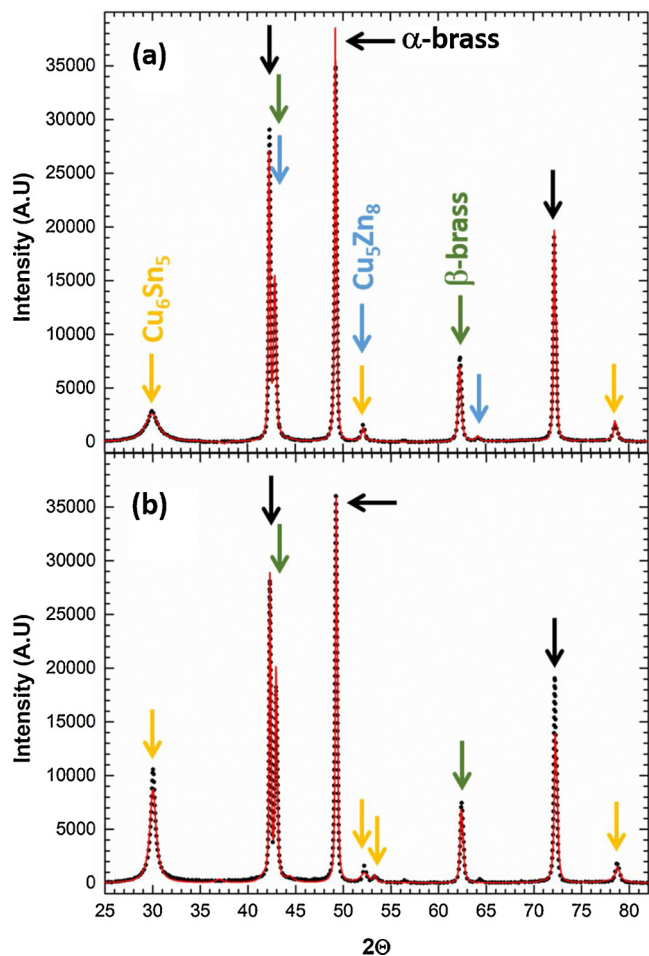


Fig. 6. Simulated (solid red line) and experimental (dotted black line) X-ray diffractograms of the Zn-bearing (a) and the Zn-free (b) bronzes. The  $\alpha$ -brass (black),  $\beta$ -brass (green),  $\text{Cu}_6\text{Sn}_5$  (yellow) and  $\text{Cu}_5\text{Zn}_8$  (blue) visible peaks are reported. (For interpretation of the references to colour in this figure legend, the reader is referred to the web version of this article.)

morphology were observed between the Zn-free and Zn-bearing samples (Table 1). This was essential for the comparison between corrosion resistances of the two coatings.

Comparative analysis of the cross-sections (e.g. Fig. 2) was performed for each sample. All the coatings were compact throughout the cross-section, well adherent to the substrate, and no voids or inhomogeneities in the morphology were observed.

Ionic images were collected after the cross-sectioning, to acquire information on the microstructure and faceting. Ionic imaging contrast is, in fact, able to quickly highlight crystal shapes by channelling effect, without the need for previous metallographic treatments. Fig. 3 shows a

Table 6  
Unit distances between samples in dE units (colour space).

dE (distance)		Zn white bronze			Zn-free white bronze			Ag
		1.5 $\mu\text{m}$	1.0 $\mu\text{m}$	0.5 $\mu\text{m}$	1.5 $\mu\text{m}$	1.0 $\mu\text{m}$	0.5 $\mu\text{m}$	
Zn white bronze	1.5 $\mu\text{m}$	0	2	2	4	6	2	18
	1.0 $\mu\text{m}$	2	0	0	2	4	1	17
	0.5 $\mu\text{m}$	2	0	0	2	4	0	17
Zn-Free white bronze	1.5 $\mu\text{m}$	4	2	2	0	2	2	15
	1.0 $\mu\text{m}$	6	4	4	2	0	4	13
	0.5 $\mu\text{m}$	2	1	0	2	4	0	17
Ag		18	17	17	15	13	17	0

Table 7  
Colour coordinates of the deposited surfaces.

Label		L	A	b
Zn white bronze	1.5 $\mu\text{m}$	91	0.7	6.8
	1.0 $\mu\text{m}$	92	0.5	4.6
	0.5 $\mu\text{m}$	91	0.7	4.9
Zn-Free white bronze	1.5 $\mu\text{m}$	93	0.4	3.6
	1.0 $\mu\text{m}$	95	0.4	3.2
	0.5 $\mu\text{m}$	91	0.3	5.1
Ag		107	0.1	-1.8

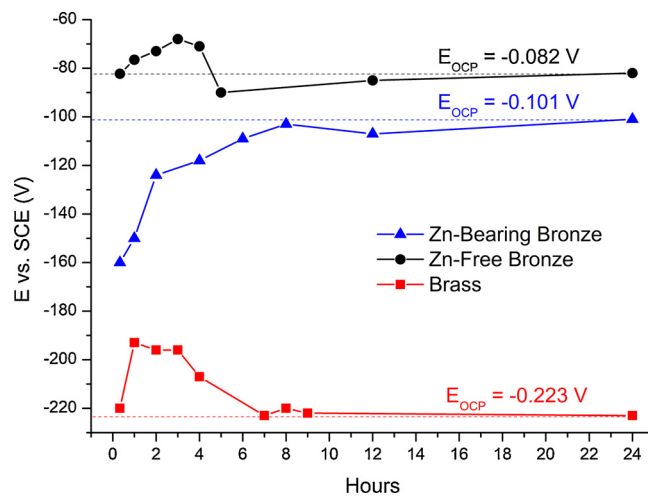


Fig. 7. 24 h OCP curves of 1 $\mu\text{m}$  samples, brass in comparison.

comparison between the cross-sections of the Zn-free (a) and Zn-bearing (b) white bronzes; the images show similar columnar growth.

### 3.1.3. Bulk composition of the coatings

Brass substrates are commonly used in mass industrial production due to their low cost, easy machining and corrosion resistance. However, due to the similar composition of the substrate and coating, the determination of the film composition is not straightforward. The presence of copper and zinc in both the substrate (brass) and the coating (bronze) hampers the use of liquid phase methods, as no chemical attack can stop at the interface between the coating and the substrate. This also prevents from using X-ray fluorescence. Indeed, small variations in the composition of the substrate generate significant errors in the estimation of the coating composition.

Oppositely, Energy-Dispersive X-ray Microanalysis can measure such composition, even if its application needs special care. For small thicknesses like the ones investigated in this study, there is the need to fine-tune the analysis condition to avoid that the interaction volume

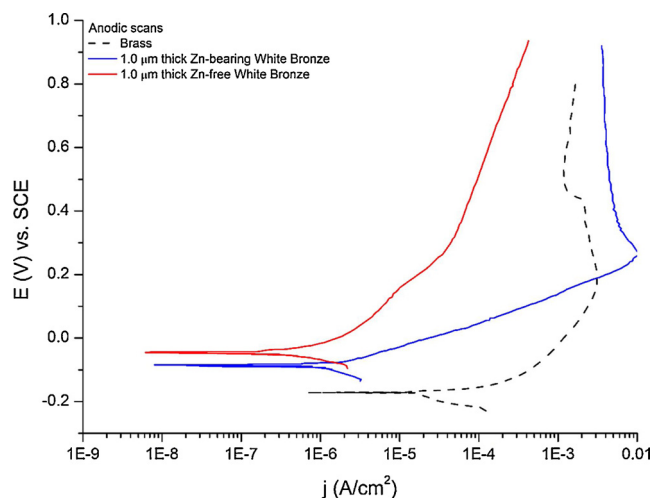


Fig. 8. Comparison between anodic sweeps of different thicknesses of Zn-bearing white bronzes (blue curve), Zn-free white bronzes (red curve) and bare brass (substrate, dotted curve).

includes the substrate. To find the conditions that maximise the signal of the coatings, while being sure that no X-ray comes from the substrate, we performed Monte Carlo simulations. Nowadays, these simulations can be readily implemented with software like DTSA II [41], PENEPMA [42] or WinXray [43]. Recently, we have shown that this approach can be applied to the simultaneous estimation of coating thickness and composition in thin films [44]. This approach has been applied here to determine the energy conditions that give the best compromise between the excitation of the Cu and Zn K-lines (energy between 8 and 9 KeV) and the need to avoid that the thickness of the interaction volume exceeds the thickness of the investigated layer (see Supplementary S1). Simulations were carried out with CASINO [45]. Calculations showed that at an excitation energy of 12 keV, the interaction volume depth is less than 300 nm. This energy excites Cu and Zn K transitions significantly. Tables 2 and 3 report the composition of the layer that has been obtained by EDX with the application of the ZAF quantification algorithm [46] along with the relative error estimation. The measurements have been repeated at ten different points of the surface. Samples with different thickness showed oscillation in Sn, Cu and Zn within 1–2 wt% (Table 2). No significant composition dependence on the thickness has been observed. In the case of the Zn-Free bronze, the Pd content showed considerable variation. However, the Pd content is in the 1% wt. range, easy to detect but hard to quantify for the low peak to background and signal to noise ratios. Table 3 shows that for both the classes of coatings are high tin bronzes, as the tin wt. % resulted in 25–26 wt.% for the Zn bearing and 36 wt. % for the Zn free.

### 3.2. Surface composition (XPS)

A comparison of the XPS peaks for all metallic elements, Oxygen and Carbon, before and after sputtering, is reported in Figs. 4 and 5. An

Table 8  
Summary of the electrochemical parameters obtained from potentiodynamic cycles.

Sample		OCP 1 [V]	Jcorr 1 [A/cm <sup>2</sup> ]	OCP 2 [V]	Jcorr 2 [A/cm <sup>2</sup> ]
Zn-bearing White Bronze	0.5 μm	-0.126	1.66 × 10 <sup>-6</sup>	-0.166	4.40 × 10 <sup>-5</sup>
	1.0 μm	-0.085	2.79 × 10 <sup>-7</sup>	-0.115	3.19 × 10 <sup>-5</sup>
	1.5 μm	-0.095	4.37 × 10 <sup>-7</sup>	-0.111	2.24 × 10 <sup>-5</sup>
Zn-Free White Bronze	0.5 μm	-0.132	4.77 × 10 <sup>-7</sup>	-0.088	2.23 × 10 <sup>-6</sup>
	1.0 μm	-0.046	1.49 × 10 <sup>-7</sup>	-0.107	2.06 × 10 <sup>-5</sup>
	1.5 μm	-0.023	5.80 × 10 <sup>-7</sup>	-0.107	1.42 × 10 <sup>-5</sup>
Brass		-0.170	1.11 × 10 <sup>-5</sup>	-0.117	3.22 × 10 <sup>-5</sup>

overview of the single peak shape for each film thickness is reported in Fig. SI2, displaying a remarkable reproducibility along with all the samples in each series. A complete summary of the surface composition is reported in Table 4.

Sample surfaces showed a composition which differs from the bulk composition found using EDX. First, in both Zn-bearing and Zn-free coatings, a significant amount of carbon and oxygen was observed. The as-deposited samples showed a significant concentration of carbon at the surface. However, the shape of the carbon peak demonstrated dissimilar contamination for the two coatings. Zn-containing bronzes were the most contaminated, suggesting that additives used in the bath remained on the surface even after cleaning with water and ultrasounds. For the Zn-bearing white bronzes, an intense signal can be attributed to C-O, in agreement with the results obtained by the morphological studies (Table 4). All samples showed a component at 286.3 eV that is typical of the polyalcohols employed as brighteners [47] (Fig. 5).

The surface of samples before sputtering showed no copper in the case of the Zn-bearing bronze. Similarly, the unsputtered Zn-free bronze showed a copper content significantly lower than what was expected from the analysis of the bulk concentration, with copper atoms in the form of oxide or hydroxide species (Cu<sup>o</sup> and Cu<sub>2</sub>O at 932.1 eV, that are not distinguishable using standard XPS analysis, and CuO at 933.4 eV [48]). Additionally, surface tin was almost completely oxidised in the Zn-free bronze (Sn<sup>o</sup> at 485.0 eV, Sn Oxides at 486.5 eV [49]), while a direct comparison with the Zn-bearing bronze showed that a more substantial fraction of tin at the surface was metallic. In these samples, Zn is in the form of oxides (Zn<sup>o</sup> at 1021.8 eV, Zn Oxide at 1022.1 eV [50]).

All the examined samples showed metal ratios much different from the bulk, with lower copper content on the surface (Table 5).

XPS acquired after sputtering showed better agreement with the result of the bulk composition (Table 2) for the Zn-free bronze samples. The concentration of zinc and tin for the Zn bronze after sputtering was still noticeable, despite a lower extent to the unsputtered samples. Pd content does not change significantly after surface sputtering, as its atomic fraction remained in line with the values acquired during EDX experiments. Moreover, we found that all the elements in bulk were in the metallic state, and the carbon contamination disappeared after sputtering. Only a small amount of carbon (less than 1 % at.) remained. Considering that after the sputtering process the superficial carbon contamination (adventitious carbon) was removed, the remaining atoms of this element can be located only on the bulk of the samples. This fact is indicating that the coatings may retain some carbon impurity as a result of the incorporation of the galvanic bath organic additives.

### 3.3. XRD measurements

To identify the crystalline structure of the coatings, we performed X-ray diffraction experiments; Fig. 6 reports the experimental diffractograms along with the simulated patterns. Typically, electrodeposited bronze consists of intermetallic compounds such as Cu<sub>6</sub>Sn<sub>5</sub> and Cu<sub>5</sub>Zn<sub>8</sub> [51,52]. The XRD of the Zn bearing and the zinc-free materials showed

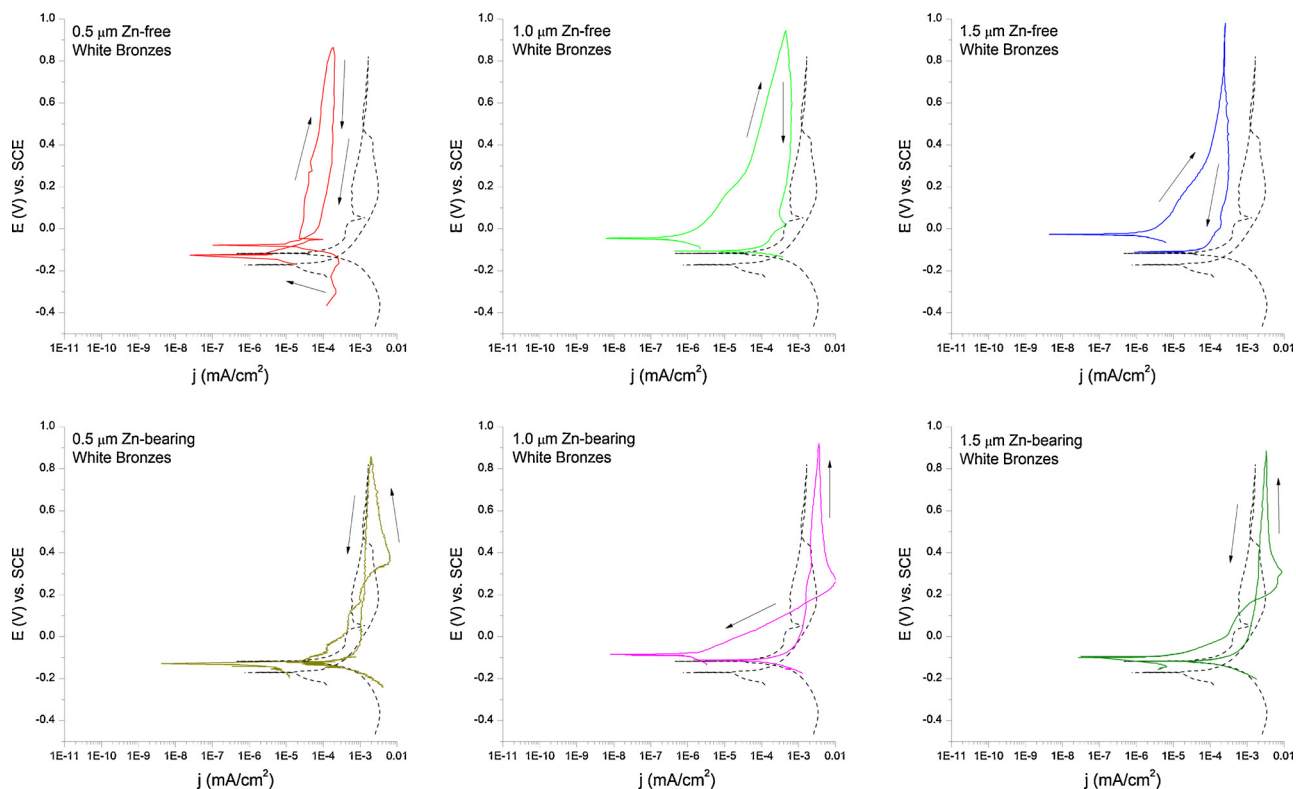


Fig. 9. Comparison between the polarisation curves of Zn-free white bronze (top row), and Zn-bearing white bronze (bottom row) electrodeposited white bronzes in a 0.62 M NaCl solution in water at pH 8.2.



Fig. 10. Zn-bearing (top row) and Zn-free (bottom row) samples after polarisation cycles; the red square indicates an almost-invisible corrosion mark for the 0.5μm Zn-free sample. (For interpretation of the references to colour in this figure legend, the reader is referred to the web version of this article.)

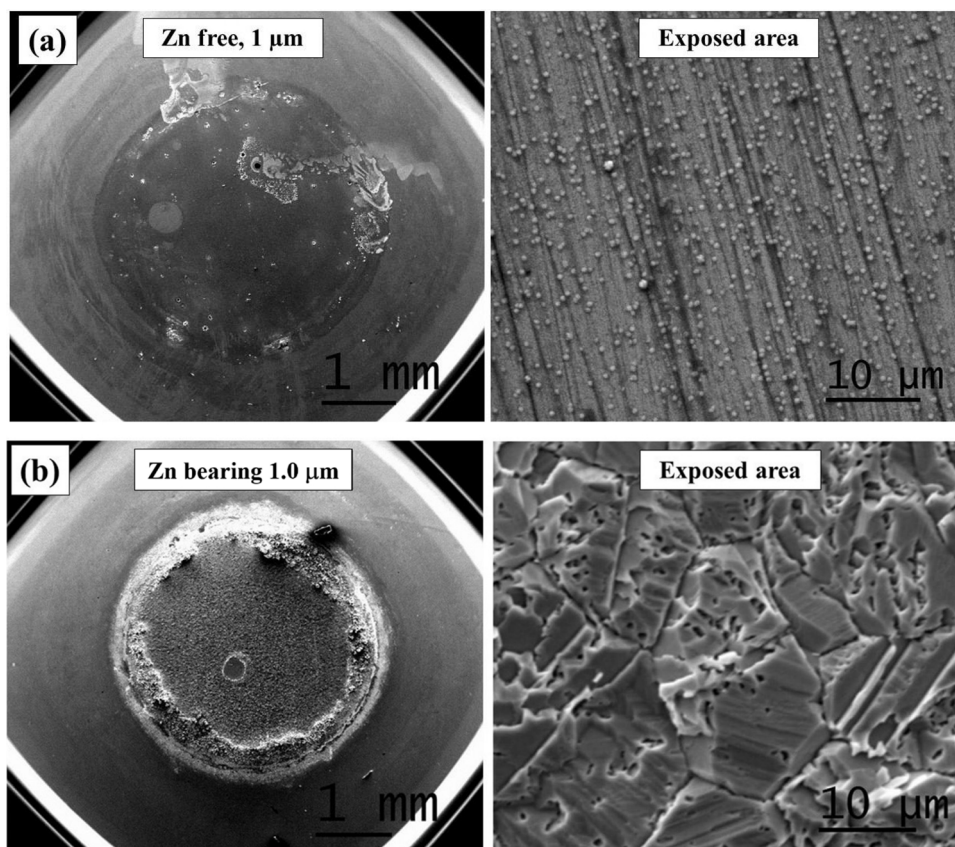


Fig. 11. SEM images of: (a) Zn-free and (b) Zn bearing white bronze samples after the polarisation cycles.

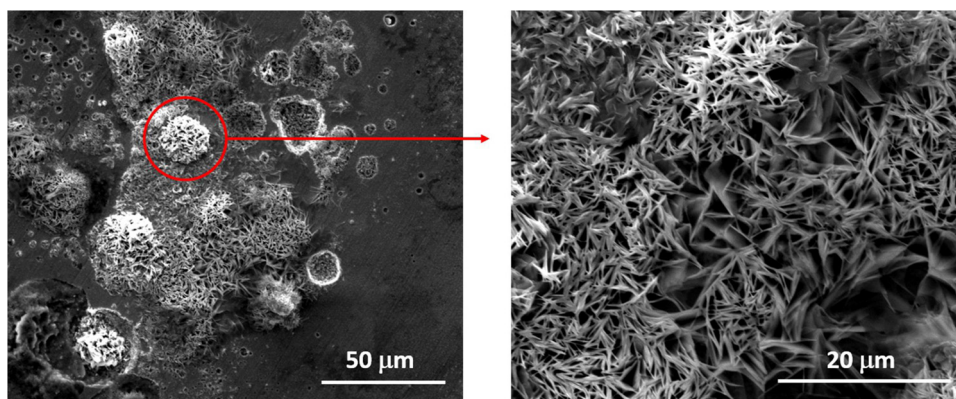


Fig. 12. (left) The surface of a Zn-free bronze sample (1 $\mu$ m thick) after polarisation tests (SEM image). A zoomed image of the flaky-like Zn structure (right) is also presented.

a peak at  $30^\circ$  due to the (101) reflection of the  $\text{Cu}_6\text{Sn}_5$  structure [53,54]. The peak fitting of the diffractogram confirmed this. The occurrence of the  $\text{Cu}_5\text{Zn}_8$  [53] phase in the Zn bearing material is harder to prove, as its peaks superimpose much with those of  $\text{Cu}_6\text{Sn}_5$  and the brass substrate (the (110) at  $\sim 42.8$  of the  $\beta$ -brass). XRD spectra simulation was performed to separate the contribution of the layers. The fit of the diffraction pattern matches (Fig. 6) the intensities of the peaks much better when the  $\text{Cu}_5\text{Zn}_8$  phase is added in the simulated spectra (Mean squared error,  $wR^2$ , is reduced from 10 % to 6 %), suggesting its presence. No Pd related peak was visible from the XRD data of the Zn-Free bronze, suggesting that the addition of a small palladium fraction does not significantly affect the coating structure.

All the recorded diffractograms clearly showed the peaks of the substrate; three peaks were attributed to the  $\alpha$ -phase, while three others to the  $\beta$ -phase. This is consistent with the phase speciation expected for

a Cu 67 wt. % and Zn 33 wt. % brass [55].

The full pattern analysis yields a crystallite size of  $70 (\pm 5)$  nm for the Zn-bearing bronze and of  $50 (\pm 5)$  for the Zn-free bronze (isotropic approximation). This finding is in agreement with SEM observations, that showed a nanometric roughness of the surface with smaller features in the case of the Zn-Free bronze. A reference diffractogram of the substrate is reported in the SI.

### 3.4. Characterization of the colour

Colour coordinates were reported in Table 6 (where unity distances between samples in colour space are shown) and in Table 7 (where, for each sample, colour coordinates are given). In the tabs also silver coordinates are reported; silver is used as a target colour for the bright whitish deposits used in the industry. All samples show a bright white

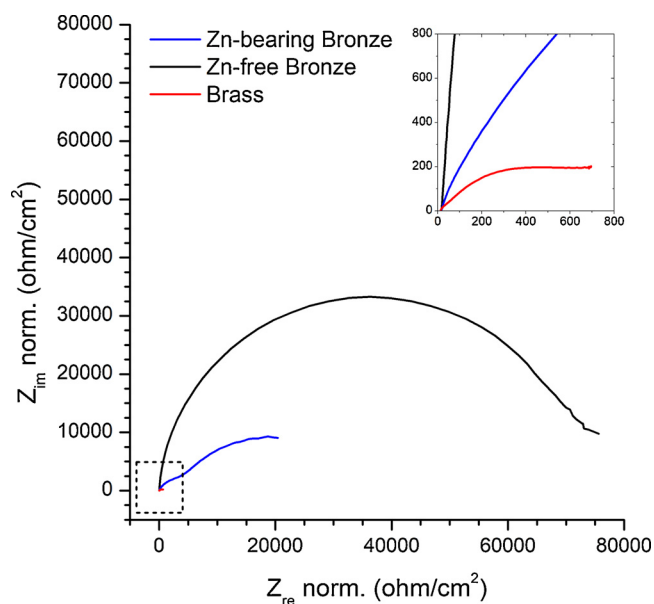


Fig. 13. Nyquist plot of 1 $\mu$ m samples and substrate brass.

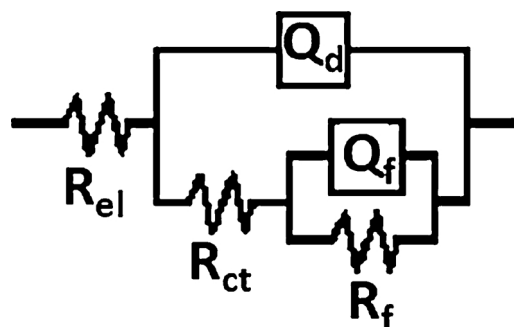


Fig. 14. The circuit used for EIS data fitting.  $R_{el}$ ,  $R_{ct}$  and  $R_f$  are respectively the electrolyte resistance, the Charge transfer resistance and the Faradic resistance.  $Q_d$  and  $Q_f$  are Constant Phase Elements related to double-layer capacitance and faradic capacitance.

colour, with a reddish hue, barely perceivable by the naked eye, and a luminosity close to the reference white. Zn white bronzes show a lower dependency of the Lab coordinates on the thickness of the coatings, having all the colour distances in the 0–2 range (not distinguishable by naked-eye observation) but a slightly more reddish colour (bigger  $a$  values, see Table 7). Zn-Free bronzes are white, but the thinner deposit (0.5  $\mu$ m) shows a noticeable difference, with the other two samples having a colour difference in the range 2–4. The former has a slightly reddish colour, more similar to the Zn white bronzes, having a colour distance from these in the range 1–2 (not distinguishable by the naked eye).

### 3.5. Electrochemical corrosion in 3.5 % sodium chloride

To determine the corrosion protection that the Zn-Free and Zn-bearing coatings give to brass, and to compare the performance of the various coatings, we performed OCP measurements, anodic polarization and Electrochemical Impedance Spectroscopy (EIS) on the surfaces in sodium chloride solution.

Fig. 7 shows the OCP data of the two 1  $\mu$ m thick samples, and of brass substrate. The curves demonstrate a nobler behaviour of the Zn-free sample compared to the Zn-bearing white bronze. Moreover, the OCP data from the two coatings differs sharply from the value obtained from the brass substrate, which is much more negative.

Fig. 8 reports the polarization curves of the white bronzes of three

different thicknesses, compared to brass. The corresponding corrosion parameters, OCPs and corrosion current densities, are listed in Table 8. From the dataset, it is clear that all the investigated coatings do prevent corrosion on the brass; indeed, all the coated samples have more positive OCPs and lower  $J_{corr}$  compared to the substrate (Table 8). On such a basis we conclude that the white bronzes behave as cathodic coatings. However, the OCPs difference between the two coatings and the uncoated brass is small. We found the largest difference (147 mV) to occur between brass and the 1.5  $\mu$ m thick-Zn-Free coating, while for the Zn bearing materials, the OCP difference with the substrate is lower than 100 mV for each film thickness, indicating a small galvanic coupling between the coating and the substrate.

We observed that at a fixed anodic potential of 0.23 V, the corrosion current of the Zn-bearing bronzes (ca.  $10^{-2}$  A cm $^{-2}$ ) is much larger compared to the Zn-Free bronze ( $10^{-5}$  A cm $^{-2}$ ). This trend is maintained in the whole anodic range of the potentiodynamic scan; Zn-Free shows a steeper slope indicating that the kinetics of the corrosion process is slower than for the Zn-bearing materials. Accordingly, the resistance to the anodic stress of the brass protected with the Zn-Free coatings significantly exceeds the resistance of the Zn bearing ones.

Additionally, we explored the effect of the thickness on the corrosion performance. To do so, we have recorded the polarization curves of the samples with a nominal thickness of 0.5, 1 and 1.5  $\mu$ m (Fig. 9). We observed that for both materials, the 0.5  $\mu$ m samples show more negative OCPs and that these are relatively close to that of brass (Table 8). The 1.0 and 1.5  $\mu$ m samples show OCP values more cathodic compared to the 0.5  $\mu$ m samples. Moreover, the maximum corrosion current density was lower in the thinnest films compared to the thicker ones (Table 8).

As the composition does not change much as a function of the thickness, we suppose that the behaviour may result from the presence of defects which discontinue the thinner coatings, exposing the brass underneath.

Fig. 10 reports the result of the visual inspection of the samples after the cyclic polarization experiments. The Zn-Free samples did not show appreciable changes after the corrosion test, retaining the original silvery appearance. In contrast, the Zn-bearing samples experienced a homogeneous corrosion process that led to a change in the colour from metallic to brown-copper.

SEM images (Fig. 11) supported the evidence of uniform corrosion in the Zn-bearing bronzes (Fig. 11b). From the images, a complete dissolution of the coating can be seen, with the uncovering of the de-zincified brass grains of the substrate. Oppositely the surfaces of the Zn-Free bronzes showed the evidence of localised corrosion phenomena (Fig. 11a), in line with what reported in the literature for bulk materials of similar composition [56]. This phenomena manifest with a bigger extent on the boundary between sample holder sealing and exposed sample surface and can be a consequence of a localized higher current density. However, copper content in an alloy is known to favour pit nucleation, when the object is immersed in a NaCl rich solution. This process is assisted by the hydrolysis of  $Sn^{4+}$  ( $Sn^{4+} + 4H_2O \rightarrow Sn(OH)_4 + 4H^+$ ). In contrast, Cu-Zn-Sn alloys with Zn content of 20 % or more initially form a Zn oxide surface layer providing some protective action, followed by dissolution in chloride media [50]. Fig. 12 also shows the formation of localised flakes in the Zn-Free sample. EDX suggests an oxygen enrichment on these structures, which is consistent with the formation of Zn oxide in the proximity of the corroded regions. The origin of the flakes is attributed to the precipitation of the dissolved zinc from the brass underneath on the surface of the sample. This demonstrates that in the Zn-Free bronze the corrosion proceeds locally on small anodic spots of uncovered brass. In contrast, the corrosion of the Zn-bearing coatings is uniform as revealed by the SEM images that, after the polarization experiments, showed the etched grain structure of the brass substrate.

A perusal of XPS data can achieve further insight into the behaviour of the coatings. All the tested samples were left in the atmosphere after

their preparation, leading to the formation of the open-air passivation patina on their surface. We found that in the Zn-free bronze the passivation layer at the surface consists mainly of tin dioxide with a little copper oxide, while in the Zn-bronze it was a mixture of various oxides of Sn and Cu and metallic Sn. From the literature, it is known that the passivation power of tin in chloride media is higher than that of Zn [57].

In the end, we performed EIS measurements, on two pristine 1  $\mu\text{m}$  thick coatings, after an hour immersion in the NaCl electrolyte. In Fig. 13, the Nyquist Plot of the two 1  $\mu\text{m}$  thick bronzes is reported. The figure shows that the sample with the highest impedance at low frequencies (less than 10 Hz) is the Zn-free. In respect to the Zn-bearing one. EIS data were fitted using a circuit with two CPE elements (Fig. 14). The model includes both charge transfer and faradic reactions above the surface, and it is widely reported in the literature for the investigation of copper alloys in NaCl aqueous solutions [58–60]. From the fitting of the data related to the two bronzes we obtained two different values for  $R_{ct}$ ; for the Zn-bearing sample, we obtained an  $R_{ct}$  of  $3.96 \times 10^3 \Omega$ , while the value for the Zn-free one was  $6.92 \times 10^4 \Omega$ . We found an  $R_{ct}$  value for the brass substrate of  $2.14 \times 10^1 \Omega$ . Small variation was seen between the two  $R_F$  values ( $3.58 \times 10^4 \Omega$  and  $3.29 \times 10^4 \Omega$  respectively, vs.  $1.93 \times 10^3 \Omega$  of the brass). The  $\chi^2$  between the fitting and the obtained data were below  $10^{-3}$  for all the samples. Both the data obtained by EIS circuit fitting, and Nyquist plot confirmed a faster corrosion rate for the Cu-Zn-Sn bronzes and a more passive electrochemical behaviour of the Zn-free sample, confirming the trends already observed in the potentiodynamic scans.

#### 4. Conclusion

In this work, we have investigated two class of electrodeposited white bronzes, one consisting of Cu, Zn, and Sn (Zn-bearing white bronze) and another consisting of Cu, Sn and a small addition of Pd (1 % wt., Zn-free white bronze).

A special focus was placed on the determination of the corrosion protection that the coatings bestow in chloride media. This point is of utmost importance as white bronzes can come in contact with chloride rich solutions in many applications, e.g. as protective layers for electrical connection for automotive or as coatings for fashion or technical clothes.

Electrochemical corrosion tests in 3.5 % NaCl, demonstrated two different corrosion mechanisms for the coatings. Zn-free coatings perform better and retain the original appearance even after the potentiodynamic testing in NaCl solution, while the Zn-bearing ones tend to corrode uniformly, reaching the brass substrate underneath. Based on the results of the XPS analysis, we suggest that the enhanced corrosion resistance provided by the Zn-free coating results from the formation of a continuous and electrochemically inert tin oxide layer at the surface. SEM inspection of the surface of the coating after the polarization tests showed the evidence of localized corrosion phenomena for these deposits. Such localized corrosion is mainly found near the circular border of the sample holder and can be a consequence of a higher current density during potentiodynamic scans. Moreover, it could be a consequence of an occasional lack of continuity in the film coverage. Oppositely, the Zn-bearing bronzes corrode uniformly with the colour of the exposed area that turns from shiny metallic to the reddish copper-like. This is due to the preferential dezincification of the surface, and the precipitation of insoluble Cu oxides and hydroxides, with the formation of a porous patina.

After 24 h the OCP value of the Zn-free sample was the least negative, followed by the Zn-bearing coated sample and by brass.

The EIS analysis confirmed the trend in corrosion resistance observed by the potentiodynamic scans. The Nyquist plots displayed that the Zn-free coating has the highest impedance in the low-frequency (< 10 Hz) range of the spectrum, indicating a slow charge transfer and highest faradaic resistance.

Our findings indicate that the Zn-free coated samples are the least corroding in chloride media and therefore, should be the favourite choice if occasional exposure to the marine atmosphere may occur. The presence of a significant amount of Zn in the layer with the concurrent reduction of tin results in a dramatic worsening of degradation phenomena.

It was still not possible to precisely assess the role of Pd in corrosion resistance; Structural investigations and surface analysis showed that the limited concentration of Pd in the Zn-free coatings do not affect the crystal structure and the surface composition of the material significantly. No Pd phase was detected by XRD measurements, suggesting no significant role of this element on the anticorrosive properties of the coating. Moreover, XPS analysis reported a slightly lower surface Pd content in respect to bulk before the sputtering process, proposing a lesser influence of this element in the anticorrosive properties of the film.

#### Declaration of Competing Interest

The authors declare that they have no known competing financial interests or personal relationships that could have appeared to influence the work reported in this paper.

#### Acknowledgements

This research was funded by Regione Toscana for POR CreO Fesr 2014–2020 GADGET project (CUP CIPE: D55F17000230009), “Ente Cassa di Risparmio di Firenze” Grant Number n. 2013.0878 and Regione Toscana POR FESR 2014–2020 for the project FELIX (Fotonica ed Elettronica Integrate per l’Industria), Grant Number 6455. The authors thank the Italian National Research Council (CNR) microscopy facility “Ce.M.E.–Centro Microscopie Elettroniche Laura Bonzi” for providing the facilities for the FIB cross-sectioning, SEM imaging and Mr Carlo Bartoli and Dr Maria Cristina Salvatici for keeping the FIB-SEM up and running and the support is given to the measurements.

#### Appendix A. Supplementary data

Supplementary material related to this article can be found, in the online version, at doi:<https://doi.org/10.1016/j.corsci.2020.108898>.

#### References

- [1] W.A.T. Dos Santos, W.I.A. Dos Santos, S.L. De Assis, M. Terada, I. Costa, Bronze as alternative for replacement of nickel in intermediate layers underneath gold coatings, *Electrochim. Acta* 114 (2013) 799–804, <https://doi.org/10.1016/j.electacta.2013.10.040>.
- [2] G. Moretti, F. Guidi, G. Capobianco, R. Tonini, Ni-free alloys as final coatings: white bronze coatings on copper, *J. Mater. Chem.* 11 (2001) 922–925, <https://doi.org/10.1039/b006401g>.
- [3] S. Caporali, U. Bardi, Corrosion mechanism in artificial sweat solution of in-bearing white bronze alloy, *Corrosion* 68 (2012), <https://doi.org/10.5006/1.3683223>.
- [4] A. Hovestad, R.A. Tacke, H.H.T. Manntje, Electrodeposited nanocrystalline bronze alloys as replacement for Ni, *Phys. Status Solidi Curr. Top. Solid State Phys.* 5 (2008) 3506–3509, <https://doi.org/10.1002/pssc.200779424>.
- [5] U. Beck, G. Reiners, I. Urban, H.A. Jehn, U. Kopacz, H. Schack, Decorative hard coatings: new layer systems without allergy risk, *Surf. Coat. Technol.* 61 (1993) 215–222, [https://doi.org/10.1016/0257-8972\(93\)90228-G](https://doi.org/10.1016/0257-8972(93)90228-G).
- [6] W. Giurlani, G. Zangari, F. Gambinossi, M. Passaponti, E. Salvietti, F. Di Benedetto, S. Caporali, M. Innocenti, Electroplating for decorative applications: recent trends in research and development, *Coatings* 8 (2018) 1–25, <https://doi.org/10.3390/coatings8080260>.
- [7] B. Unveroglu, G. Zangari, Effect of cell configuration on the compositional homogeneity of electrodeposited Cu-Zn-Sn alloys and phase purity of the resulting Cu<sub>2</sub>ZnSnS<sub>4</sub> absorber layers, *Electrochim. Acta* 255 (2017) 347–357, <https://doi.org/10.1016/j.electacta.2017.08.155>.
- [8] S. Ahmed, K.B. Reuter, O. Gunawan, L. Guo, L.T. Romankiw, H. Deligianni, A high efficiency electrodeposited Cu<sub>2</sub>ZnSnS<sub>4</sub> solar cell, *Adv. Energy Mater.* 2 (2012) 253–259, <https://doi.org/10.1002/aenm.201100526>.
- [9] H. Streiberger, K. Dössel, *Automotive Paints and Coatings*, Wiley, 2008, <https://doi.org/10.1002/9783527622375>.
- [10] H. Lipowsky, E. Arpaci, *Copper in the Automotive Industry*, Wiley, 2006, <https://doi.org/10.1002/9783527622375>.

- doi.org/10.1002/9783527611652.
- [11] T. Hreid, J. Li, Y. Zhang, H.J. Spratt, H. Wang, G. Will, Effects of metal ion concentration on electrodeposited CuZnSn film and its application in kesterite Cu<sub>2</sub>ZnSnS<sub>4</sub> solar cells, *RSC Adv.* 5 (2015) 65114–65122, <https://doi.org/10.1039/c5ra09966h>.
- [12] D.M. Berg, A. Crossay, J. Guillot, V. Izquierdo-Roca, A. Pérez-Rodríguez, S. Ahmed, H. Deligianni, S. Siebentritt, P.J. Dale, Simplified formation process for Cu<sub>2</sub>ZnSnS<sub>4</sub>-based solar cells, *Thin Solid Films* 573 (2014) 148–158, <https://doi.org/10.1016/j.tsf.2014.11.012>.
- [13] L. Guo, Y. Zhu, O. Gunawan, T. Gokmen, V.R. Deline, S. Ahmed, L.T. Romankiw, H. Deligianni, Electrodeposited Cu<sub>2</sub>ZnSnS<sub>4</sub> thin film solar cell with 7% power conversion efficiency, *Prog. Photovolt. Res. Appl.* 22 (2014) 58–68, <https://doi.org/10.1002/pip.2332>.
- [14] R. Juškenas, G. Niaura, Z. Mockus, S. Kanapeckaitė, R. Giraitis, R. Kondrotas, A. Naujokaitis, G. Stalnis, V. Pakštas, V. Karpavičiūtė, XRD studies of an electrochemically co-deposited Cu-Zn-Sn precursor and formation of a Cu<sub>2</sub>ZnSnS<sub>4</sub> absorber for thin-film solar cells, *J. Alloys Compd.* 655 (2016) 281–289, <https://doi.org/10.1016/j.jallcom.2015.09.186>.
- [15] N. Mandich, Cyanide copper plating reinvents itself, *Met. Finish.* 103 (2005) 30–36, [https://doi.org/10.1016/S0026-0576\(05\)80077-7](https://doi.org/10.1016/S0026-0576(05)80077-7).
- [16] S. Xing, *Environmentally Friendly Baths for Cu-Sn Co-Electrodeposition: Cyanide-Free Aqueous Bath and Deep Eutectic Solvents*, PhD thesis Environ. Friendly Baths Cu-Sn Co-Electrodeposition Cyanide-Free Aqueous Bath Deep Eutectic Solvents, 2014.
- [17] N. Piccinini, G.N. Ruggiero, G. Baldi, A. Robotto, Risk of hydrocyanic acid release in the electroplating industry, *J. Hazard. Mater.* 71 (2000) 395–407, [https://doi.org/10.1016/S0304-3894\(99\)00089-8](https://doi.org/10.1016/S0304-3894(99)00089-8).
- [18] M.P. Mordechay Schlesinger, *Modern Electroplating*, John Wiley & Sons, Inc., Hoboken, NJ, USA, 2010, <https://doi.org/10.1002/9780470602638>.
- [19] Y. Fujiwara, H. Enomoto, Electrodeposition of β-brass from cyanide baths with accumulative underpotential deposition of Zn, *J. Electrochem. Soc.* 147 (2000) 1840–1846, <https://doi.org/10.1149/1.1393444>.
- [20] Y.D. Gamburg, G. Zangari, *Theory and Practice of Metal Electrodeposition*, Springer, New York, New York, NY, 2011, <https://doi.org/10.1007/978-1-4419-9669-5>.
- [21] E. Bertorelle, *Trattato di Galvanotecnica*, Hoepli, 2016.
- [22] H. Strow, Brass and bronze plating, *Met. Finish.* 105 (2007) 163–167, [https://doi.org/10.1016/S0026-0576\(07\)80330-8](https://doi.org/10.1016/S0026-0576(07)80330-8).
- [23] E. Brian, *Studies of Bronze Electrodeposition*, (1992).
- [24] E.W. Brooman, Corrosion behavior of environmentally acceptable alternatives to nickel coatings, *Met. Finish.* 99 (2001) 100–102, [https://doi.org/10.1016/S0026-0576\(01\)81296-4](https://doi.org/10.1016/S0026-0576(01)81296-4).
- [25] C. Powell, P. Webster, *Copper Alloys for Marine Environments*, (2011), p. 33.
- [26] V. Callcut, Section 7 – BRASSES FOR CORROSION RESISTANCE, in: *COPPER DEVELOPMENT ASSOCIATION* (Ed.), *Brasses – Prop. Appl.* – Pub 117, 1996, pp. 45–60 <https://copperalliance.org.uk/knowledge-base/resource-library/brasses-properties-applications/>.
- [27] S.B. Lyon, Corrosion of Tin and its Alloys, *Shreir's Corros.* (2010), pp. 2068–2077, <https://doi.org/10.1016/B978-044452787-5.00099-8>.
- [28] J. Muller, B. Laik, I. Guillot, Cu-Sn bronzes in sulphate medium: influence of the tin content on corrosion processes, *Corros. Sci.* 77 (2013) 46–51, <https://doi.org/10.1016/j.corsci.2013.07.025>.
- [29] S. Sohn, T. Kang, The effects of tin and nickel on the corrosion behavior of 60Cu-40Zn alloys, *J. Alloys Compd.* 335 (2002) 281–289, [https://doi.org/10.1016/S0925-8388\(01\)01839-4](https://doi.org/10.1016/S0925-8388(01)01839-4).
- [30] G.A. El-Mahdy, Electrochemical impedance study on brass corrosion in NaCl and (NH<sub>4</sub>)<sub>2</sub>SO<sub>4</sub> solutions during cyclic wet-dry conditions, *J. Appl. Electrochem.* 35 (2005) 347–353, <https://doi.org/10.1007/s10800-004-8347-1>.
- [31] C. Kleber, M. Schreiner, Multianalytical in-situ investigations of the early stages of corrosion of copper, zinc and binary copper/zinc alloys, *Corros. Sci.* 45 (2003) 2851–2866, [https://doi.org/10.1016/S0010-938X\(03\)00113-6](https://doi.org/10.1016/S0010-938X(03)00113-6).
- [32] A. Altomare, N. Corriero, C. Cuocci, A. Falcicchio, A. Moliterni, R. Rizzi, QUALX2.0: a qualitative phase analysis software using the freely available database POW-COD, *J. Appl. Crystallogr.* 48 (2015) 598–603, <https://doi.org/10.1107/S1600576715002319>.
- [33] B.H. Toby, R.B. Von Dreele, GSAS-II: the genesis of a modern open-source all purpose crystallography software package, *J. Appl. Crystallogr.* 46 (2013) 544–549, <https://doi.org/10.1107/S0021889813003531>.
- [34] J.L. Taylor, *Taylor, Reflectance Measurements of Materials Used in the Solar Industry Selecting the Appropriate Accessories for UV / Vis / NIR Measurements*, Perkin elmer Technical Note, Shelton, USA, 2009.
- [35] A. Giaccherini, *Multispectra Software*, (2019) (Accessed 7 February 2020), <https://github.com/AndreaGiaccherini>.
- [36] M. Sjödh, ColorMath—a package for color summed calculations in SU(N c), *Eur. Phys. J. C* 73 (2013) 2310, <https://doi.org/10.1140/epjc/s10052-013-2310-4>.
- [37] I.C. on Illumination, *Colorimetry – Part 4: CIE 1976 L \* a \* B \* COLOUR*, (2007).
- [38] L. Oniciu, L. Mureşan, Some fundamental aspects of levelling and brightening in metal electrodeposition, *J. Appl. Electrochem.* 21 (1991) 565–574, <https://doi.org/10.1007/BF01024843>.
- [39] A.L. Portela, G.I. Lacconi, M. Lo, Nicotinic acid as brightener agent in copper electrodeposition, *J. Electroanal. Chem.* 495 (2001) 169–172.
- [40] A. Survila, Z. Mockus, S. Kanapeckaitė, D. Bražinskienė, R. Juškenas, S. Kanapeckaitė, D. Bražinskienė, R. Juškenas, Surfactant effects in Cu-Sn alloy deposition, *J. Electrochem. Soc.* 159 (2012) D296–D302, <https://doi.org/10.1149/2.084205jes>.
- [41] N.W.M. Ritchie, J. Davis, D.E. Newbury, DTSA-II: a new tool for simulating and quantifying EDS spectra - application to difficult overlaps, *Microsc. Microanal.* 14 (2008) 1176–1177, <https://doi.org/10.1017/S143192760808361X>.
- [42] X. Llovet, F. Salvat, PENEPMA: a monte carlo program for the simulation of X-ray emission in electron probe microanalysis, *Microsc. Microanal.* 23 (2017) 634–646, <https://doi.org/10.1017/S1431927617000526>.
- [43] H. Demers, P. Horny, R. Gauvin, E. Lifshin, WinX-ray: A new Monte Carlo program for the simulation of X-ray and charging materials, *Microsc. Microanal.* 8 (2002) 1498–1499, <https://doi.org/10.1017/s1431927602104120>.
- [44] W. Giurlani, E. Berretti, M. Innocenti, A. Lavacchi, Coating thickness determination using X-ray fluorescence spectroscopy: Monte Carlo simulations as an alternative to the use of standards, *Coatings* 9 (2019) 79, <https://doi.org/10.3390/coatings9020079>.
- [45] P. Hovington, D. Drouin, R. Gauvin, CASINO: a new monte carlo code in C language for electron beam interaction -part I: description of the program, *Scanning* 19 (2006) 1–14, <https://doi.org/10.1002/sca.4950190101>.
- [46] J.I. Goldstein, D.E. Newbury, P. Echlin, D.C. Joy, C.E. Lyman, E. Lifshin, L. Sawyer, J.R. Michael, *Quantitative X-ray analysis: the basics*, Scanning Electron Microsc. X-Ray Microanal. Springer US, Boston, MA, 2003, pp. 391–451, [https://doi.org/10.1007/978-1-4615-0215-9\\_9](https://doi.org/10.1007/978-1-4615-0215-9_9).
- [47] P.G. Rouxhet, M.J. Genet, XPS analysis of bio-organic systems, *Surf. Interface Anal.* 43 (2011) 1453–1470, <https://doi.org/10.1002/sia.3831>.
- [48] G. Ertl, R. Hierl, H. Knözinger, N. Thiele, H.P. Urbach, XPS study of copper aluminate catalysts, *Appl. Surf. Sci.* 5 (1980) 49–64, [https://doi.org/10.1016/0378-5963\(80\)90117-8](https://doi.org/10.1016/0378-5963(80)90117-8).
- [49] L. Kövér, Z. Kovács, R. Sanjinés, G. Moretti, I. Csery, G. Margaritondo, J. Pálincás, H. Adachi, Electronic structure of tin oxides: high-resolution study of XPS and Auger spectra, *Surf. Interface Anal.* 23 (1995) 461–466, <https://doi.org/10.1002/sia.740230705>.
- [50] G. Deroubaix, P. Marcus, X-ray photoelectron spectroscopy analysis of copper and zinc oxides and sulphides, *Surf. Interface Anal.* 18 (1992) 39–46, <https://doi.org/10.1002/sia.740180107>.
- [51] P.L. Cavallotti, L. Nobili, A. Vicenzo, Phase structure of electrodeposited alloys, *Electrochim. Acta* 50 (2005) 4557–4565, <https://doi.org/10.1016/j.electacta.2005.03.060>.
- [52] O. Girin, E. Alloy, I. Phase, M. Material, P. Composition, Phase and structure formation of metallic materials electrodeposited via a liquid state stage: new experimental proof, *Defect Diffus. Forum* 304 (2010) 99–105 [10.4028/www.scientific.net/DDF.303-304.99](https://doi.org/10.4028/www.scientific.net/DDF.303-304.99).
- [53] G. Petzow, E.T. Henig, H.L. Lukas, F. Aldinger, A. Prince, *Comprehensive handbook of ternary alloy phase diagrams*, *Bull. Alloy Phase Diagr.* 1 (1980) 36–40, <https://doi.org/10.1007/BF02881177>.
- [54] W.X. Lei, Y. Pan, Y.C. Zhou, W. Zhou, M.L. Peng, Z.S. Ma, CNTs – Cu composite layer enhanced Sn – Cu alloy as high performance anode materials for lithium-ion batteries, *RSC Adv.* (2014) 3233–3237, <https://doi.org/10.1039/c3ra44431g>.
- [55] A.G. Guy, *Elements of Physical Metallurgy*, (1951), <https://doi.org/10.1002/bbpc.19520560927>.
- [56] I. Constantinides, A. Adriaens, F. Adams, Surface characterization of artificial corrosion layers on copper alloy reference materials, *Appl. Surf. Sci.* 189 (2002) 90–101, [https://doi.org/10.1016/S0169-4332\(02\)00005-3](https://doi.org/10.1016/S0169-4332(02)00005-3).
- [57] H.G. Spilker, G. Jänsch-Kaiser, N. Pérez, Copper-zinc alloys (brass), *Corros. Handb.* Wiley-VCH Verlag GmbH & Co. KGaA, Weinheim, Germany, 2012, <https://doi.org/10.1002/9783527610433.chb281016> p. NA-NA.
- [58] K. Marušić, H.O. Čurković, E.S. Lisac, H. Takenouti, Two imidazole based corrosion inhibitors for protection of bronze from urban atmospheres, *Croat. Chem. Acta* 91 (2018) 435–446, <https://doi.org/10.5562/cca3440>.
- [59] K. Marušić, H.O. Čurković, H. Takenouti, Inhibiting effect of 4-methyl-1-p-tolyimidazole to the corrosion of bronze patinated in sulphate medium, *Electrochim. Acta* 56 (2011) 7491–7502, <https://doi.org/10.1016/j.electacta.2011.06.107>.
- [60] K. Marušić, H.O. Čurković, H. Takenouti, Corrosion inhibition of bronze and its patina exposed to acid rain, *J. Electrochem. Soc.* 160 (2013) C356–C363, <https://doi.org/10.1149/2.063308jes>.